Analytical Field and Torque Analysis of a Reaction Sphere

Zhu, Linyu; Guo, Jian; Gill, Eberhard

DOI
10.1109/TMAG.2018.2871386

Publication date
2018

Document Version
Accepted author manuscript

Published in
IEEE Transactions on Magnetics

Analytical Field and Torque Analysis of a Reaction Sphere

Linyu Zhu, Jian Guo, and Eberhard Gill

Faculty of Aerospace Engineering, Delft University of Technology, 2629HS Delft, The Netherlands

In recent years, the increasing need in small satellite solutions triggers the miniaturization of attitude control systems. Reaction spheres were proposed as promising replacements of conventional reaction wheels for their 4π rotations. Since the generated control torques could be about any desired axes, a single reaction sphere is sufficient for three-axis stabilizations of spacecraft. This paper presents an innovative design of reaction spheres. Its driving unit is a combination of permanent magnets (PMs) and electromagnetic induction. This enables the generation of torques about three principle axes simultaneously. Meanwhile, a contactless bearing is integrated into the actuator design. Detailed designs and working principles of the reaction sphere are described. To investigate performance characteristics of the actuator, field modeling is of great importance and provides the basis for dynamics modeling. In this paper, an improved analytical model for dynamic fields excited by slotless distributed windings is presented for the first time. To study the cross coupling between PMs and electromagnetic induction, the static field generated by PMs is also modeled analytically. These developed models are validated through comparisons with numerical simulations. Electromagnetic torques generated by the actuator are calculated through the approaches of the Maxwell stress tensor and the Lorentz force law. Torque calculations based on the analytical field models deviate from those based on the numerical model slightly, with the maximum error within 4%. This means the presented analytical models allow to predict the electromagnetic field distribution and torques precisely.

Index Terms— **Analytical model, electromagnetic induction, magnetic field, reaction sphere.**

I. Introduction

REACTION wheels are commonly used actuators in spacecraft attitude control systems (ACS). Compared to magnetorquers and thrusters, they typically provide a higher control accuracy [1]. In general, to achieve three-axis stabilizations of spacecraft, at least three wheels are required. Nevertheless, for small spacecraft where volume resources are limited, it is challenging to mount three wheels on-board. In addition to volume conflicts, low power requirements trigger various innovations. A majority of the innovations offer the advantage of multi-degree of freedom (DOF). Actually, reaction spheres are special three-DOF reaction wheels which can rotate about any desired axes and generate torques about three principle axes simultaneously. Therefore, a single reaction sphere is sufficient for three-axis stabilizations without redundancy.

Although reaction spheres have been proposed a half century ago [2], there is none ready for space applications yet. The difficulty of designing a reaction sphere mainly stems from integration, miniaturization, and control aspects. For instance, some designs integrate multi-DOF into a single actuator by distributed poles [3]–[5]. Due to the strong coupling between each other, all the poles will be controlled independently and cooperatively to perform the desired rotations. Besides, the transient state of the rotor is a necessity in the control algorithm and it is normally estimated through measurements of the magnetic flux density distribution. For time delays caused by processing of noisy measurements, estimations, and control algorithms, the achievable maximum speed of the actuator is restricted [6]. Within spherical actuators which are capable of continuous rotations about at least three independent axes, the maximum speed of arbitrary axis rotations hardly exceeds 1000 r/min [7]. In addition, the rotation requires a proper bearing which may introduce interferences to the driving unit. For example, reaction spheres proposed in [8] and [9] achieved magnetic levitation and single-axis rotation simultaneously. However, the 3-D rotations were implemented with air bearings [10], since the suspension flux introduces disturbance torques. The drawback of air bearings is that the continuous air supply complicates its implementation for space missions. Even though the multi-DOF could be relatively decoupled from each other and from the bearing in special cases [10], [11], retaining a decent power efficiency and dimensional ratio between the rotor and the stator is challenging. If the input stator current density keeps constant in the scaling down of an electromagnetic machine, the torque generation capability decreases faster than the copper loss. The resultant efficiency deteriorates. Besides, the installation of sensors requires space and presents another limit in the miniaturization of reaction spheres.

To avoid the low effectiveness of 3-D induction motors and the complicated control brought by distributed permanent magnet (PM) poles, an innovative design of reaction spheres is proposed in this paper. Different from existing designs, it combines PMs and electromagnetic induction together (see Fig. 1). Meanwhile, contactless support is integrated in the driving unit. In Section II, the structure and working mechanism of the actuator is described in detail. To facilitate dynamics modeling, analytical models for the involved electromagnetic fields are developed and validated through comparisons with numerical models. An important contribution of this paper is the improved analytical model for dynamic fields excited by slotless distributed windings. Compared to models presented in [12]–[14], the component of B_θ is maintained here, which provides a further insight about the field distribution and flux leakage in spherical actuators. Based on the obtained field information, electromagnetic forces and torques acting on the rotor can be calculated fast and accurately.

Manuscript received May 16, 2018; revised July 25, 2018; accepted September 3, 2018. Corresponding author: J. Guo (e-mail: J. Guo@tudelft.nl).

Color versions of one or more of the figures in this paper are available online at http://ieeexplore.ieee.org.

Digital Object Identifier 10.1109/TMAG.2018.2871386

TABLE I
DESIGN REQUIREMENTS OF THE REACTION SPHERE

Requirements	Value [unit]
Temperature range	$-20°$C to $+50°$C
Mass	1 kg
Size	100 mm$\times$ 100 mm$\times$ 100 mm
Power consumption	15 W(max.)/ 3 W(nominal)
Max. torque	15 mNm
Speed range	2 rpm to 8,000 rpm
Resolution of speed control	1 rmp
Tilt angle	4π

Although cross couplings exist between PMs and the electromagnetic induction, they can be handled properly by the control of bearing coils. Therefore, rotations excited by the electromagnetic induction are relatively decoupled from other DOF and can be modeled like those of conventional asynchronous machines. Dynamics modeling of the reaction sphere goes beyond the scope of this paper and will be presented in a subsequent paper.

II. PRELIMINARY DESIGN OF THE REACTION SPHERE

The spherical actuator is designed for ACS of microsatellites (mass $\leq$ 100 kg). Considering the general working environments of microsatellites, attitude control requirements, mass, and power budgets etc. requirements listed in Table I will be used to guide the design. Please note that the angular momentum storage capability is not included in the table for two reasons. First, with the same mass or the same volume, a cylinder could provide a larger moment inertia than a sphere, due to the mass distribution. Therefore, if the maximum spinning speeds are the same, reaction spheres do not show advantages over reaction wheels regarding the momentum storage capability. The main benefit of a reaction sphere is its reconfigurable rotation axis (or the direction of output torques). Analysis on the functionality is the primary objective of the study. Second, to simplify the prototyping and mitigate the risk of rotor unbalance, the rotor is designed to be a solid sphere. Optimization of moment inertia with a hollow sphere is planned for the later study phase.

To enable 4π rotations, a majority of existing reaction spheres utilize PM poles or electromagnetic induction to generate driving torques [7]. Compared with other electromagnetic machines, induction motors have no fixed poles on the rotor. The motion of the rotor mainly depends on the energized windings. When multiple revolving magnetic fields are excited, rotations about a composite axis will be generated. However, in such cases, cross couplings exist in the flux distribution and the generation of torques about different axes, and result in unwanted eddy currents. These unwanted eddy currents cause heating, decrease the efficiency, and may introduce vibrations [15]. By contrast, PM machines have fixed poles on the rotor. Torques are generated by the interaction between PM poles and energized electromagnets. It means that the generated torque depends on the rotor's transient orientation, which complicates the motion control [16].

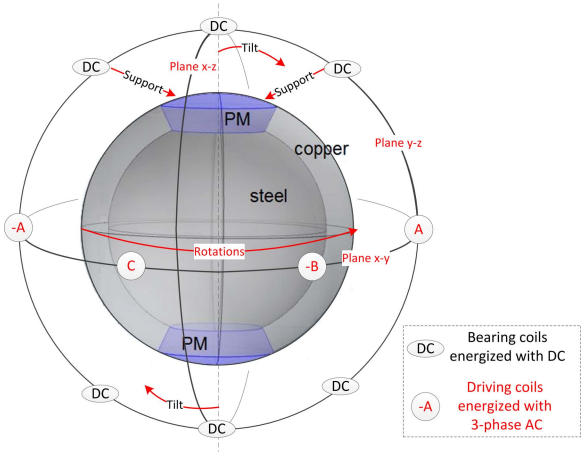

Fig. 1. Working principle of the proposed reaction sphere.

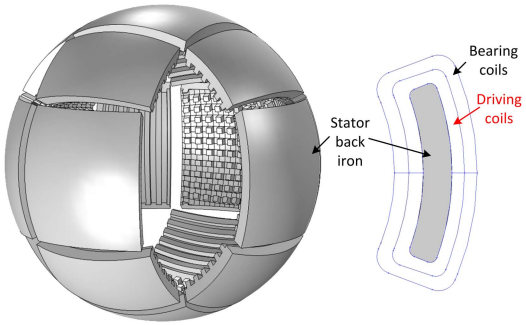

Fig. 2. Assembled stator back iron where driving coils and bearing coils are wound around.

In addition, 4π rotations require a special topology of the multiple PM poles and electromagnets [7].

To avoid problems mentioned earlier, the proposed reaction sphere combines both PMs and electromagnetic induction within the driving unit. Normally, the rotation is about the axis of symmetry of the PMs and is driven by induced eddy currents. The actuator provides control torques through accelerations and decelerations. A benefit of the design is that the axis of symmetry is configurable. This is realized through interactions between the two surface-mounted PMs on the rotor and energized bearing coils on the stator. To mitigate the coupling between electromagnetic induction and PMs, the PMs are mounted such that like-poles are pointing outwards. Meanwhile, interactions between PMs and activated bearing coils provide a contactless support to the rotor.

Fig. 1 illustrates the basic working principle of the proposed reaction sphere. To ensures the rotor orientation, speed, and position are always under control, three sets of windings are placed on the stator orthogonally (not all involved coils are illustrated in Fig. 1). Each set is arranged about a principle axis, consisting of three pairs of driving coils and six pairs of bearing coils. To reduce the axial length, stator windings are wound toroidally around the stator back iron. One set of driving windings placed about the z-axis is illustrated in Fig. 5 in Section V-A. Arrangement of the driving windings is similar to that of a three-phase ac machine. Bearing coils are placed coaxially with the driving coils, and they are controlled in pairs to drive tilts or translational displacements. Fig. 2 shows how windings about three principle axes are wound and assembled

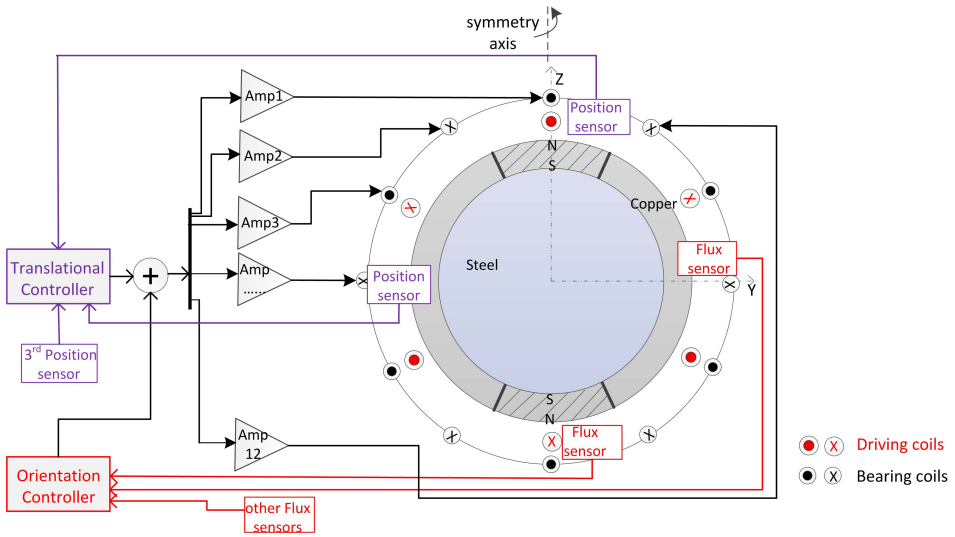

Fig. 3. Position and orientation control of the rotor.

together. For clarity, one piece of stator segment is removed in Fig. 2. Please note that slots on the inner surface of the stator back iron do not really exist. They are drawn here to illustrate the way wires are wound (i.e., flowing directions of carried stator currents). At the joint of two winding sets, winding would be wound around the same stator iron segment. It is important to note that the dimensional ratio between driving coils and bearing coils in Fig. 2 does not mean the real ratio. Although the employed toroidal coils [17], [18] shortens the axial length of stator windings, the electrical conductor length is not reduced. Consequently, the stator resistance and copper loss on the windings are not decreased.

Fig. 3 shows loops for the magnetic suspension and orientation control when the symmetry axis is along the z-axis. Energizing one pair of bearing coils (oppositely placed) with opposite dc inputs results in a translational force. Therefore, with at least three pairs of bearing coils interacting with the PMs, translational displacements of the rotor can be controlled. When the pair of bearing coils are provided with the same dc input current, electromagnetic torques are generated. For orientation controls, several bearing coils will be activated subsequently. Actually, detailed control of bearing coils depends on the rotor orientation and torque/force calculations are complicated. Although tilt through the 4 π range is allowed by the design, the bearing control efficiency is not isotropic. It depends on the relative orientation of the rotor with respect to energized bearing coils. In operations, the transient rotor orientation will be estimated through mounted 2-D Hall sensors. The sensors are inserted to the reaction sphere through the gaps between stator segments (see Fig. 2). Dynamics modeling and bearing control of the proposed reaction sphere are expected in a future paper.

When the symmetry axis is along the principle axes (x-, y-, and z-axes), rotations excited by the electromagnetic induction are as with the conventional asynchronous machines. If the symmetry axis deviates from the principle axes through the orientation control, rotations about the symmetry axis can be realized by energizing more than one set of ac windings [11].

III. Magnetic Field Modeling

In contrast to numerical analysis, analytical analysis offers a deep insight into the mechanism. Especially for 3-D problems, a numerical simulation may take hours, while the analytical model will give a result within minutes. The essence of analytical magnetic field modeling is solving Maxwell's equations. Generally, the quasi-static approximation can be applied to the electromagnetic fields of electric machines [19]. It assumes that capacitive effects in the machine are negligible, which in turn simplifies Maxwell's equations.

To model magnetic fields, a basic way is to calculate and integrate the magnetic flux density produced by each charge or small segment of currents. However, boundary conditions are not considered in this method [20]. In real machines, boundaries exist and the magnetic field is the result of PMs, changing electric fields and magnetized ferrimagnets. In some cases, the boundaries can be removed via the image method [21]. Nevertheless, that is not always feasible. A more general approach is introducing variables, e.g., magnetic potentials, transforming Maxwell's equations to Laplace's or Poisson's equations for separated regions. Unknowns in the general solutions can be solved by boundary conditions. Alternatively, mapping methods such as the Schwarz–Christoffel transformation and magnetic equivalent circuit [22] can be useful but are limited to special cases [20].

Since the proposed actuator will be excited to perform 4π rotations, the magnetic field modeling is a 3-D problem. Besides, the spherical geometry facilitates the analysis in a spherical frame, where the general solution to Laplace's equations is known. Therefore, the approach of transforming Maxwell's equations to Laplace's/Poisson's equations is adopted in this paper.

A. Assumptions

The analytical model of the spherical actuator is based on the following assumptions.

1) The stator is slotless.

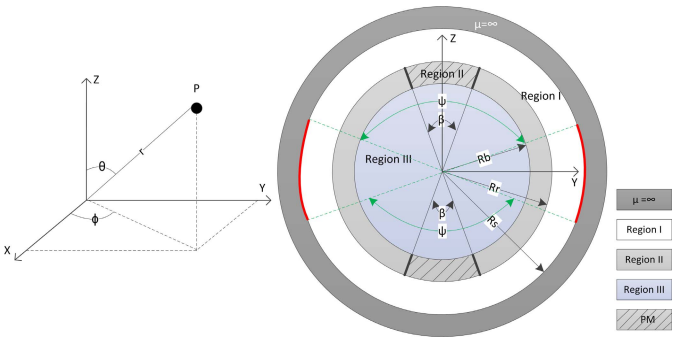

Fig. 4. Geometry of the reaction sphere.

2) No eddy currents in the stator back iron.
3) No high-order time or space harmonics.
4) The relative permeability of iron is infinite.
5) Only one set of driving windings is excited at a certain time.
6) No saturation of iron.
7) End effects are neglected.
8) PMs have a linear demagnetization characteristic and are fully magnetized in the direction of magnetization.
9) The actuator is in mechanical and electrical steady states.
10) Electromagnetic couplings between stator windings are negligible.

B. Parameters

The simplified geometry of the reaction sphere is shown in Fig. 4. The whole actuator is axial symmetric. For convenience, a spherical coordinate system is employed with its origin at the rotor core. On the rotor, PMs (in gray with slash) and the copper domain (in gray) form region II. Region III is the steel core, while region I refers to air surrounding the rotor. Stator windings are modeled as surface currents $\vec{J}_f = J_0 \cos(\omega t - \phi)/\sin\theta \cdot \vec{e_\theta}$ distributed on the inner surface of the stator shell within the region of $\theta \in [\psi/2, \pi - \psi/2]$. Design of the reaction sphere starts with a dimensional ratio of 1:9 between the rotor and the whole actuator [7]. As per the size requirement listed in Table I, the external radius of the rotor R_r is determined. Table II lists the dimensional parameters and basic inputs of the reaction sphere. Many parameters in Table II are results of conflicting preferences. For instance, a large space between the stator and the rotor accommodates more windings and higher input currents. However, space occupied by the stator windings extends the effective air gap width and weakens the coupling between the rotor and the stator. Therefore, the geometrical parameters listed here are only for the preliminary design and will be optimized later.

The spherical actuator is designed with a maximum rotational speed of 8000 r/min. For a two-pole induction machine, the speed of 8000 r/min requires an input frequency of no less than 140 Hz. However, with the nominal phase voltage, if the input frequency is high, the stator and rotor reactance will be high. Consequently, the achievable maximum torque will be low. Besides, an adjustable rotational speed is required for the actuator. Therefore, the reaction sphere will be inverter-fed operated with variable frequencies. Another benefit of the inverter-fed machine is that the rotor always runs at a small slip, which means the high starting currents can be avoided. Here, it is assumed that the actuator will start with an input frequency of 10 Hz.

TABLE II
BASIC PARAMETERS OF THE ACTUATOR

Param	Value	Meaning
R_b	20 mm	Radius of the solid rotor core (steel)
R_r	25 mm	External radius of the copper layer
β	$2 \times 25°$	Cone angle of one PM pole
R_s	30 mm	Inner radius of the stator back iron
ψ	$2 \times 65°$	Angular area without stator currents
B_r	0.23 T	Remanence of PMs

IV. ANALYTICAL FIELD MODELS

As mentioned earlier, both PMs and excited driving windings are involved in this actuator. PMs generate a static field, while the ac driving windings generate a time-harmonic field. To simplify the analysis, the composite field is separated into three time harmonics: e^{0*t}, $e^{j\omega t}$, and $e^{-j\omega t}$.

A. Static Field Generated by the PM Poles

The constitutive equations for regions I, II, and III are given in the following.

1) For region I, the magnetic property of air (or vacuum in space) is described as

$$\vec{B}_{\rm I} = \mu_0 \vec{H}_{\rm I}. \tag{1}$$

2) For region II, the PM is modeled as [23]

$$\vec{B}_{\rm II} = \mu_0 \mu_m \vec{H}_{\rm II} + \mu_0 \vec{M} \tag{2}$$

where μ_m is the relative recoil permeability and $\vec{M} = \vec{B}_r/\mu_0$ is the residual magnetization. For hard ferrites, the typical value of μ_m is 1.03–1.3 [24]. In this paper, the value is set to 1.05. On the rotor, there are two-pole pairs. Each pair is composed of one PM pole and one consequent pole. The copper space between PMs is assumed to be occupied by unmagnetized PM material ($\vec{M} = \vec{0}$) [25]. Indeed, pure copper is diamagnetic and its relative permeability is 0.999994 [26]. Nevertheless, compared to the relative recoil permeability of 1.05 for PMs, influence of the approximation is negligible.

3) For region III, the magnetic property of steel is described by

$$\vec{B}_{\rm III} = \mu_0 \mu_r \vec{H}_{\rm III}. \tag{3}$$

The relative permeability μ_r is set to 30 in this case.

Since the magnetic field generated by PMs is constant, no eddy currents are induced in the conductive domain. To minimize the number of variables and simplify calculations, the scalar magnetic potential Φ is introduced. Transforming

Maxwell's equations to Laplace's and Poisson's equations, we obtain the governing equations for each domain

$$\nabla^2\Phi_{\rm I} = 0 \tag{4a}$$

$$\nabla^2\Phi_{\rm II} = \frac{\nabla\cdot\vec{M}}{\mu_m} \tag{4b}$$

$$\nabla^2\Phi_{\rm III} = 0. \tag{4c}$$

The governing equations are solved in spherical coordinates. For regions I and III (i = I, III), the general solution to Laplace's equation is obtained through separation of variables [27]

$$\Phi_i(r,\theta,\phi) = \sum_{n=0}^{\infty}\sum_{m=-n}^{\infty}\left[\kappa_{ni}^m\cdot r^n + \xi_{ni}^m\cdot r^{-(n+1)}\right]Y_n^m(\theta,\phi) \tag{5}$$

where $Y_n^m(\theta,\phi)$ is the spherical harmonic function and κ_{ni}^m and ξ_{ni}^m are unknown constants.

Since the actuator geometry is axial symmetric, the magnetic scalar potential is independent on ϕ, which means $m = 0$ in (5). Hence, the general solution to Laplace's equation can be simplified

$$\Phi_i(r,\theta) = \sum_{n=0}^{\infty}[\kappa_{ni}\cdot r^n + \xi_{ni}\cdot r^{-(n+1)}]P_n(\cos\theta). \tag{6}$$

For region II, the general solution to Poisson's equation is obtained by adding a particular solution which satisfying the excitation item in (4b) to (6).

It is assumed that PMs are radially magnetized. Therefore, $M_\theta = M_\phi = 0$ and

$$M_r = \begin{cases} M & \text{if } \theta\in\left[0,\dfrac{\beta}{2}\right] \text{ or } \left[\pi-\dfrac{\beta}{2},\pi\right] \\ 0 & \text{if } \theta\in\left[\dfrac{\beta}{2},\pi-\dfrac{\beta}{2}\right]. \end{cases} \tag{7}$$

M_r is a piecewise function of θ and sectionally continuous in $[0,\pi]$. It can be expanded in Fourier–Legendre series [28]

$$M_r(\theta) = F_r(\cos\theta) = \sum_{n=0}^{\infty} C_{rn}P_n(\cos\theta) \tag{8}$$

with the coefficients

$$C_{rn} = \begin{cases} (2n+1)\displaystyle\int_0^{\frac{\beta}{2}} M P_n(\cos\theta)\sin\theta\ \mathrm{d}\theta & \text{if } n = \text{even}; \\ 0 & \text{if } n = \text{odd}. \end{cases} \tag{9}$$

Assume that a particular solution for region II can be written as

$$\Phi_{\rm II}^p = \sum_{n=0,2,4\cdots}^{\infty} C_1 r P_n(\cos\theta) + \sum_{n=1,3,5\cdots}^{\infty} C_2 r P_n(\cos\theta) \tag{10}$$

to meet Poisson's equation

$$\nabla^2\Phi_{\rm II}^p = \frac{\nabla\cdot\vec{M}}{\mu_m}.$$

Comparing the respective items on the both sides results in $C_1 = 2C_{rn}/[\mu_m(2-n^2-n)]$ and $C_2 = 0$.

To solve unknowns in the general solution, following boundary conditions [29] are applied:

1) finite-field condition at $r = 0$;
2) continuous radial component of $\vec{B}$ at $r = R_b$ and R_r;
3) continuous tangential components of $\vec{H}$ at $r = R_b$ and R_r;
4) $\vec{H} = \vec{0}$ inside the stator shell.

B. Time-Harmonic Field Excited by Stator Currents

Here, we focus on the dynamic field with components of $e^{j\omega t}$ and $e^{-j\omega t}$. Contrary to the static field, the residual magnetization of region II plays little role in the dynamic field. However, eddy currents are induced. In fact, the conductivity of PMs is much lower than that of copper. Since stator currents are concentrated in the low latitude area, no much difference will be caused by assuming that PMs has the same conductivity with copper.

The constitutive relation for the three domains is the same with those listed for the static field except that the residual magnetization is absent. Due to the currents, the magnetic vector potential $\vec{A}$ is introduced rather than a scalar potential. Using $\vec{A}$, Maxwell's equations are transformed to Laplace's equations for regions I and III, and the diffusion equation for region II

$$\nabla^2\vec{A}_{\rm I} = 0 \tag{11a}$$

$$\nabla^2\vec{A}_{\rm II} = \mu_0\mu_m\sigma\frac{\partial\vec{A}_{\rm II}}{\partial t} \tag{11b}$$

$$\nabla^2\vec{A}_{\rm III} = 0. \tag{11c}$$

Considering $\vec{A}$ is a vector function of r, θ, ϕ, and t, two approaches can be used to solve the governing equations. The first one is to solve the three scalar components of $\vec{A}$ separately and connect them by $\nabla\cdot\vec{A} = 0$. Another alternative is to introduce a second-order potential $\vec{W}$ and change $\nabla^2\vec{A}$ to $\nabla^2\vec{W}$ [30].

To minimize the number of variables, the second approach is adopted. The definition of the second-order magnetic potential is provided in the following [30]:

$$\begin{aligned}\vec{A} &= \nabla\times\vec{W} \\ \vec{W} &= W_1\vec{r} + \vec{r}\times\nabla W_2.\end{aligned} \tag{12}$$

It is demonstrated in [31] that $W_2 \equiv 0$ for eddy current problems. Therefore, W_2 will be omitted in the following. The second-order potential will be written as $\vec{W} = W\vec{r}$. Based on the derivation in [30] [equation 7.04(3) and (4)], governing equations with $\vec{A}$ can be converted to

$$\nabla^2\vec{A} = \nabla\times(\vec{r}\nabla^2 W) \tag{13a}$$

$$\frac{\partial\vec{A}}{\partial t} = \frac{\partial}{\partial t}[\nabla\times(\vec{r}W)] = \nabla\times\left(\vec{r}\frac{\partial W}{\partial t}\right). \tag{13b}$$

To distinguish the second-order potentials for the three domains, subscripts are added

$$\nabla^2\vec{A}_{\rm I} = 0 \ \Rightarrow \nabla^2\ W_{\rm I} = 0$$

$$\nabla^2\vec{A}_{\rm II} = \mu_0\mu_m\sigma\frac{\partial\vec{A}_{\rm II}}{\partial t} \Rightarrow \nabla^2\ W_{\rm II} = \mu_0\mu_m\sigma\frac{\partial W_{\rm II}}{\partial t}$$

$$\nabla^2\vec{A}_{\rm III} = 0 \Rightarrow \nabla^2\ W_{\rm III} = 0.$$

The magnetic flux density is formulated as

$$\vec{B} = \nabla \times \vec{A} = -\vec{r}\nabla^2 W + \nabla W + \nabla(\vec{r} \cdot \nabla W). \tag{14}$$

In this paper, a revolving magnetic field is generated. If the input currents and the winding distribution are perfectly sinusoidal, the magnetic flux density distribution shall just contain the fundamental component. This means both $\vec{B}$ and W can be expressed as functions of r, θ, and $\cos(\omega t - \phi)$, where ω is the angular frequency of input currents. To facilitate the analysis, the electric and magnetic fields are written in complex form, e.g., $e^{j\omega t}$. In fact, these fields only have the real part. Hence, the $e^{-j\omega t}$ element is additionally introduced to remove the imaginary part through Euler's formula. In the following, the subscript + and − indicates the $e^{j\omega t}$ and $e^{-j\omega t}$ elements, respectively.

1) Region I

$$W_{\mathrm{I}} = W_{\mathrm{I}+} + W_{\mathrm{I}-} \text{ With } \begin{cases} \nabla^2 W_{\mathrm{I}+} = 0 \\ \nabla^2 W_{\mathrm{I}-} = 0. \end{cases} \tag{15}$$

2) Region II

$$W_{\mathrm{II}} = W_{\mathrm{II}+} + W_{\mathrm{II}-} \text{ With } \begin{cases} \nabla^2\ W_{\mathrm{II}+} = \mu_0\mu_m\sigma \dfrac{\partial W_{\mathrm{II}+}}{\partial t} \\ \nabla^2\ W_{\mathrm{II}-} = \mu_0\mu_m\sigma \dfrac{\partial W_{\mathrm{II}+}}{\partial t}. \end{cases} \tag{16}$$

3) Region III

$$W_{\mathrm{III}} = W_{\mathrm{III}+} + W_{\mathrm{III}-} \quad \text{With} \begin{cases} \nabla^2\ W_{\mathrm{III}+} = 0 \\ \nabla^2\ W_{\mathrm{III}-} = 0. \end{cases} \tag{17}$$

General solutions to Laplace's equations in spherical coordinates have been provided in (5). For regions I and III (i = I, III)

$$\begin{aligned} W_{\mathrm{I}+} &= \sum_{n=0}^{\infty}\sum_{m=-n}^{n}\left[A_{ni}^m r^n + B_{ni}^m r^{-(n+1)}\right]Y_n^m(\theta,\phi)e^{j\omega t} \\ W_{\mathrm{I}-} &= \sum_{n=0}^{\infty}\sum_{m=-n}^{n}\left[C_{ni}^m r^n + D_{ni}^m r^{-(n+1)}\right]Y_n^m(\theta,\phi)e^{-j\omega t}. \end{aligned} \tag{18}$$

For region II, the diffusion equations will be changed to modified Helmholtz equations by defining the complex coefficients $a^2 = j\omega\mu_0\mu_m\sigma$ and $b^2 = -j\omega\mu_0\mu_m\sigma$

$$\begin{aligned} \nabla^2\ W_{\mathrm{II}+} &= j\omega\mu_0\mu_m\sigma W_{\mathrm{II}+} = a^2 W_{\mathrm{II}+} \\ \nabla^2\ W_{\mathrm{II}-} &= -j\omega\mu_0\mu_m\sigma W_{\mathrm{II}-} = b^2 W_{\mathrm{II}-} \end{aligned}$$

The general solutions to modified Helmholtz equations in a spherical frame are [32] ($i_n(ar)$ and $k_n(ar)$ are modified spherical Bessel functions)

$$\begin{aligned} W_{\mathrm{II}+} &= \sum_{n=0}^{\infty}\sum_{m=-n}^{n}\left[A_{n2}^m i_n(ar) + B_{n2}^m k_n(ar)\right]Y_n^m(\theta,\phi)e^{j\omega t} \\ W_{\mathrm{II}-} &= \sum_{n=0}^{\infty}\sum_{m=-n}^{n}\left[C_{n2}^m i_n(br) + D_{n2}^m k_n(br)\right]Y_n^m(\theta,\phi)e^{-j\omega t}. \end{aligned} \tag{19}$$

Unknowns in the general solution are solved through boundary conditions listed in Section IV-A. Please note that at $r = R_s$, the tangential component of $\vec{H}$ is discontinuous due to the surface currents within $\theta \in [\psi/2, \pi - \psi/2]$

$$H_{\mathrm{I}\phi}|_{r=R_s} = \frac{J_0}{\sin\theta}\cos(\omega t - \phi).$$

With high-order time and space harmonics neglected, $\vec{B}$ and W are functions of r, θ, and $\cos(\omega t - \phi)$. Therefore, the item $e^{j\omega t}$ only has the component of $m = -1$, while the item $e^{-j\omega t}$ only has the component of $m = 1$. Through further derivations, the boundary condition at $r = R_s$ results in

$$\sum_{n=0}^{\infty}\left[(n+1)A_{n1}^{-1}R_s^{n-1} - nB_{n1}^{-1}R_s^{-(n+2)}\right]\frac{Y_n^1(\theta,\phi)}{\mu_0} = \frac{e^{j\phi}J_0}{2j} \tag{20a}$$

$$\sum_{n=0}^{\infty}\left[(n+1)C_{n1}^{1}R_s^{n-1} - nD_{n1}^{1}R_s^{-(n+2)}\right]\frac{Y_n^1(\theta,\phi)}{\mu_0} = \frac{e^{j\phi}J_0}{2j}. \tag{20b}$$

To help solve unknowns, the right sides of (20a) and (20b) are expanded through spherical harmonics. For (20a) within the range of $\theta \in [\psi/2, \pi - \psi/2]$, we set

$$f(\theta,\phi) = \frac{\mu_0 J_0 e^{j\phi}}{2j} = \sum_{n=0}^{\infty} N_n^{-1} Y_n^1(\theta,\phi) \tag{21}$$

where

$$\begin{aligned} N_n^{-1} &= \int_0^{\pi}\int_0^{2\pi} f(\theta,\phi)Y_n^{1*}(\theta,\phi)\sin\theta\ \mathrm{d}\phi\mathrm{d}\theta \\ &= \frac{\mu_0 J_0}{2j}\sqrt{\frac{(2n+1)\pi}{n(n+1)}} \\ &\quad \cdot\left[\sin\theta P_n(\cos\theta)|_{\psi/2}^{\pi-\psi/2} - \int_{\psi/2}^{\pi-\psi/2} P_n(\cos\theta)\cos\theta\ \mathrm{d}\theta\right]. \end{aligned} \tag{22}$$

For each order n, the right sides of (23a) and (23b) are known

$$(n+1)A_{n1}^{-1}R_s^{n-1} - nB_{n1}^{-1}R_s^{-n-2} = N_n^{-1} \tag{23a}$$

$$(n+1)C_{n1}^{1}R_s^{n-1} - nD_{n1}^{1}R_s^{-n-2} = N_n^{1}. \tag{23b}$$

Combining (23a) and (23b), with boundary conditions of finite field at $r = 0$, continuous B_r and continuous H_ϕ at $r = R_b$ and R_r, all unknowns in the general solutions are solved.

V. Validation and Comparison

A. Numerical Simulations for the Static Field

To validate the analytical solutions, numerical models are built in COMSOL. Corresponding to Fig. 4, geometry of the numerical model is presented in Fig. 5. The objective of the study is the comparison of numerical and analytical results for the magnetic flux density distribution in the air gap. To enable the comparison, several half-circular curves are selected randomly to check the magnetic flux density distribution on the curves. Since the analytical solution is axial

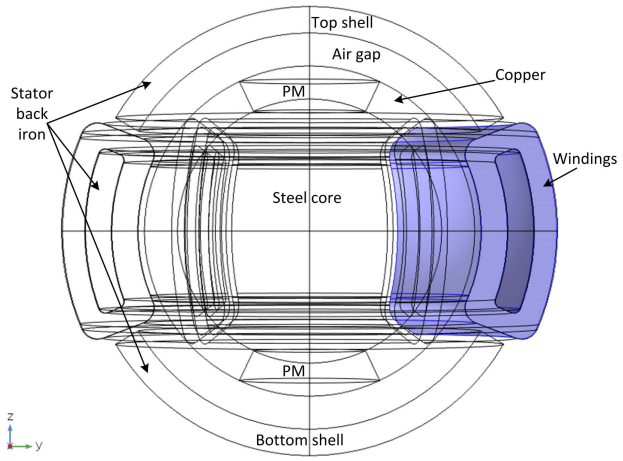

Fig. 5. Numerical model developed in COMSOL (with one driving coil highlighted).

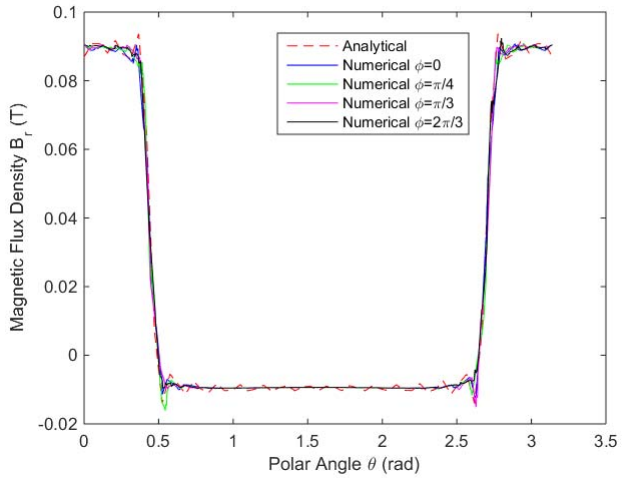

Fig. 6. Comparison of B_r on curves with various ϕ angles ($r = 25.2$ mm and $\theta \in [0, \pi]$).

symmetric, curves with different azimuth angles ϕ shall have the same magnetic flux density distribution.

The comparison of B_r is shown in Fig. 6 and B_θ in Fig. 7. The analytical result indicates $B_\phi = 0$, while the numerical results on the selected curves show an average standard deviation of 3.7×10^{-4} T, which is two orders smaller than the magnitudes of B_r and B_θ. In the finite element method based simulations, the accuracy of results depends on the element order, size, and the truncation error. Since PMs have a different remanence with the adjacent domains, the first derivative of the magnetic flux density is discontinuous and causes glitches in the graphs. For this reason, the comparison is conducted on the curve with $r = 25.2$ mm. On the rotor surface of $r = 25$ mm, the glitches are more notable. In the analytical simulations, the accuracy of this paper depends on the number of orders (n) employed in the Fourier–Legendre expansion for M_r. Given the above differences, the comparison validates that the static field generated by the PMs is axial symmetrical.

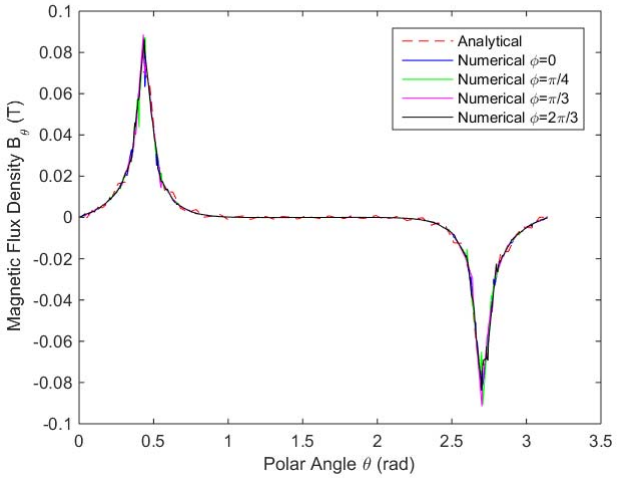

Fig. 7. Comparison of B_θ on curves with various ϕ angles ($r = 25.2$ mm and $\theta \in [0, \pi]$).

TABLE III
PARAMETERS FOR THE NUMERICAL SIMULATION

Parameters	Value
Turn number per phase per pole	N=270
Input AC current magnitude	I_0=2 A
Input AC current frequency	10 Hz
Thickness of the stator back iron	4 mm
The mechanical angle a driving coil spans	ζ=56π/180
Stator wire	AWG 23
Location of stator windings (within R_s)	r$\in$ [26, 30] mm
Physical air-gap width	1.0 mm

B. Numerical Simulations for the Dynamic Field

Parameters used in the numerical simulation are listed in Table III. To activate the electromagnetic induction, ac windings (placed on the xy plane in Fig. 1) are energized. As mentioned earlier, the energized stator windings are approximated by surface current density $\vec{J}_f = J_0 \cos(\omega t - \phi)/\sin\theta \cdot \vec{e_\theta}$ within the region of $\theta \in [\psi/2, \pi - \psi/2]$. The magnitude J_0 is derived from

$$\vec{J}_f = (I_A N_A + I_B N_B + I_C N_C) \cdot \vec{e_\theta}$$

where $I_A = I_0 \cos(\omega t)$, $I_B = I_0 \cos(\omega t - 2\pi/3)$, and $I_C = I_0 \cos(\omega t - 4\pi/3)$ are input currents for the three-phase windings. With high-order space harmonics neglected, N_A, N_B, and N_C are fundamental elements in the Fourier expansion of each phase winding distribution.

For example, the winding distribution of phase A within the region of $\theta \in [\psi/2, \pi - \psi/2]$ is described in the stator frame as

$$N'_a(\phi) = \begin{cases} -N'/\sin\theta & \text{if } \phi \in [-\zeta/2, \zeta/2] \\ N'/\sin\theta & \text{if } \phi \in [\pi - \zeta/2, \pi + \zeta/2] \end{cases}$$

where $N' = N/(\zeta R_s)$. The minus sign means when the winding is energized with I_0, the carried currents flow along the negative $\vec{e_\theta}$ direction within Region I. $N'_a(\phi)$ is approximated

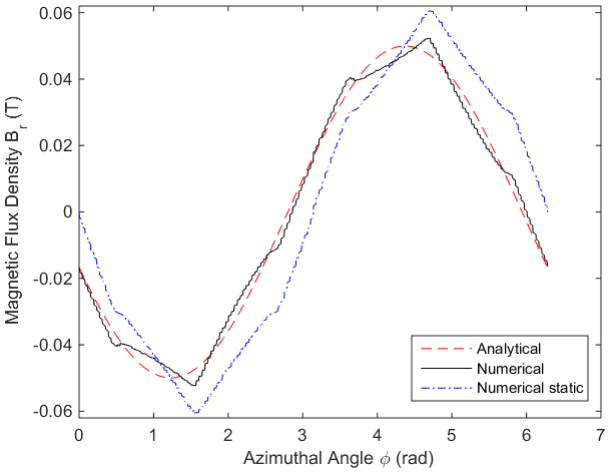

Fig. 8. Comparison of B_r on the first curve ($r = 25$ mm, $\theta = \pi/2$, and $\phi \in [0, 2\pi]$).

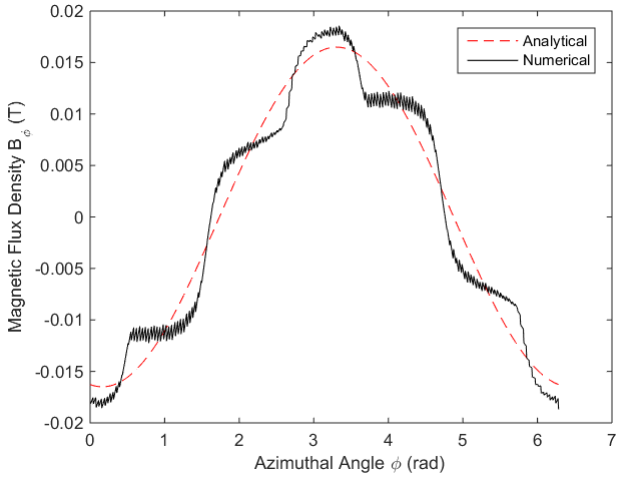

Fig. 9. Comparison of B_ϕ on the first curve ($r = 25$ mm, $\theta = \pi/2$, and $\phi \in [0, 2\pi]$).

by Fourier series

$$N'_a(\phi) = \sum_{n=1}^{\infty} a_n \cos(n\phi)/\sin\theta$$

where

$$a_n = \frac{1}{\pi}\int_{-\pi}^{\pi} N'_a(\phi)\cos(n\phi)d\phi = -\frac{2\ N'}{n\pi}\sin(\zeta/2) - \frac{2\ N'}{n\pi}\sin(\pi - \zeta/2).$$

Therefore, the fundamental element is $N_A = a_1\cos(\phi)/\sin\theta$. In the same way, $N_B = a_1\cos(\phi - 2\pi/3)/\sin\theta$ and $N_C = a_1\cos(\phi - 4\pi/3)/\sin\theta$. With the balance three-phase input currents, the magnitude of $\vec{J}_f$ is derived to be $J_0 = 1.5\ I_0\ a_1 \approx -16\,513$ A/m.

Similar to Section V-A, several curves are picked up to study the magnetic flux density distribution in the air gap. Since the remanence of PMs is set to zero in this simulation case, glitches caused by the discontinuous first derivative of the flux density disappear. The results comparison is conducted on the rotor surface $r = 25$ mm for the finner mesh there. Comparisons for B_r and B_ϕ on the first curve ($r = 25$ mm, $\theta = \pi/2$, and $\phi \in [0, 2\pi]$) are shown in Figs. 8 and 9. The analytical result indicates $B_\theta = 0$ on the selected curve, while the numerical result gives a standard deviation of 1.98×10^{-4} T (two orders smaller than the magnitudes of B_r and B_ϕ). Comparisons for $\vec{B}$ on the second curve ($r = 25$ mm, $\phi = \pi/4$, and $\theta \in [0, \pi]$) are presented in Figs. 10–12. Since the electromagnetic field is revolving, the magnetic flux density distribution at the time instant of $t = 0.1$ s is analyzed.

C. Discussions on the Dynamic Field

Through comparisons of the analytical and numerical results, it is validated that modeling the stator currents as ac surface current is principally reasonable. However, there are slight differences between the analytical and numerical results.

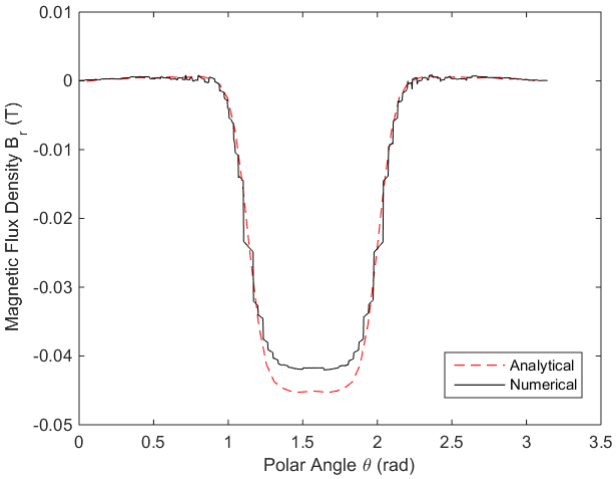

Fig. 10. Comparison of B_r on the second curve ($r = 25$ mm, $\phi = \pi/4$, and $\theta \in [0, \pi]$).

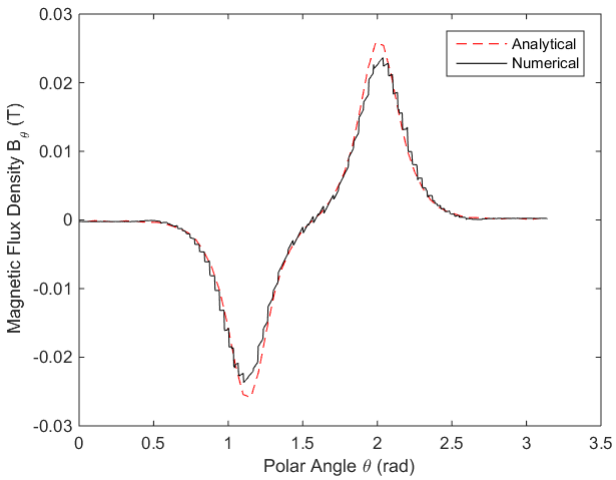

Fig. 11. Comparison of B_θ on the second curve ($r = 25$ mm, $\phi = \pi/4$, and $\theta \in [0, \pi]$).

In Fig. 8, the numerical results for B_r do not exactly follow a sinusoidal function. Instead, deformations are observed around the maximum and the minimum. To explain this phenomenon, Br distribution in the static field generated by dc inputs

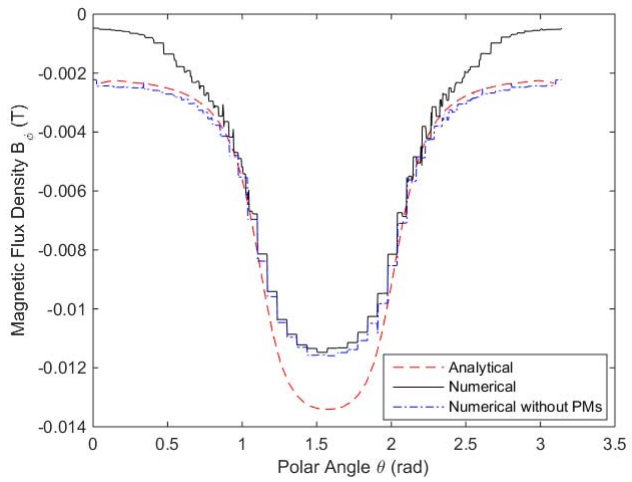

Fig. 12. Comparison of B_ϕ on the second curve ($r = 25$ mm, $\phi = \pi/4$, and $\theta \in [0, \pi]$).

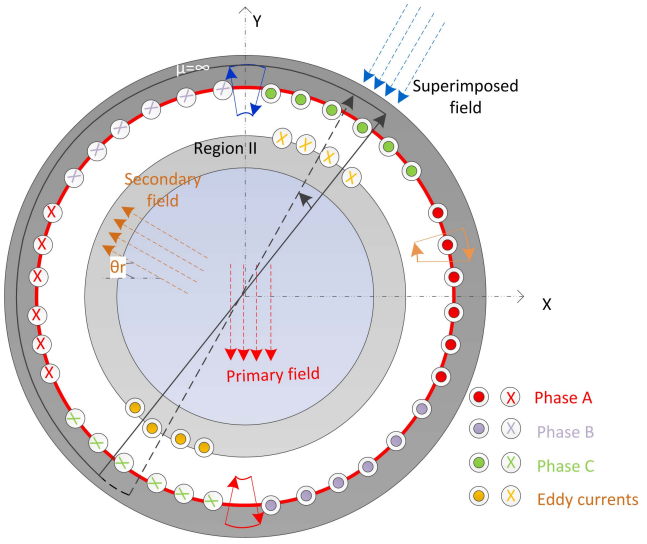

Fig. 13. Superposition of the primary and secondary fields due to eddy currents.

($I_B = I_C = -I_A/2 = -1$ A, equivalent to the inputs of ac windings at $t = 0.1$ s) is presented in Fig. 8 too. It is notable that B_r in the dynamic field is ahead of the static field in phase. Besides, its distribution is out of shape at the top parts. Actually, both deviations are caused by eddy currents.

At $t = 0.1$ s, the direction of the primary magnetic field (excited by stator currents) is along the negative y-axis (see Fig. 13). As per Lentz's law, eddy currents will be induced in the copper with the axis broadly opposite to that of stator currents. The angular displacement θ_r is determined by the rotor time constant. As a result, the secondary field generated by eddy currents changes the primary field. It makes the max. B_r direction ahead of that in the primary field.

To explain deformations of the B_r distribution, a semicircle contour is used (see Fig. 13). As per Ampere's law, $\oint_C \vec{H} \cdot \vec{\tau} dC = i_{\text{inc}}$. Since $\vec{H}$ is zero inside the stator back iron, the integration of H_r along the straight line is determined by the inclosed currents. However, when the straight line of the contour sweeps through the area where eddy currents and stator currents have opposite directions, the increase /decrease of inclosed stator currents is partially cancelled out by eddy currents. Therefore, in such areas (for instance $0.9 - \pi/2$ rad), the magnitude of B_r in the dynamic field is smaller than that in the static field. In the analytical model, both stator currents and eddy currents are sinusoidally distributed. However, in the numerical model, space harmonics exist in the winding distribution. Therefore, when the straight line of the contour sweeps, the change of inclosed currents is not sinusoidal. This reason contributes to the deformation around the maximum and the minimum.

For the B_ϕ distribution in Fig. 9, the numerical result exhibits an imperfect sinusoidal curve due to the non-sinusoidally distributed windings. A small contour above the positive x-axis is drawn in Fig. 13 for illustration. The angle of the contour is so small that we assume the integration of $\vec{H}$ along the two straight sides cancels each other out and H_ϕ in the air gap depends on the inclosed stator currents solely. Therefore, step changes of the B_ϕ distribution occur at the interfaces of different winding phases. Sparks in Fig. 9 are due to different mesh sizes used for winding domains and gaps between winding domains. In addition, both the analytical and numerical results in Fig. 9 show a slight phase lag from a negative cosine wave. Actually, although the angle of the contour is very small, the integrations of $\vec{H}$ along the two straight sides do no counteract each other completely. For instance, at $\phi = \pi/2$, H_r is negative and its magnitude at the right side (in Fig. 13) is larger than the left side due to the shafted B_r distribution in the superimposed field (It is better illustrated by the analytical results in Fig. 8). Hence, the integration of $\vec{H}$ along the two sides results in a positive value and H_ϕ in the air gap is negative. Similarly, H_ϕ in the air gap is positive at $\phi = -\pi/2$. Hence, a slight phase shift is generated.

B_θ components in Fig. 11 are mainly caused by stator leakages. In the numerical model, the stator back iron is not a complete shell. Gaps exist between the top/bottom shells and the iron wound with windings (see Fig. 5). At the axial ends of the stator windings, the magnetic flux path to the top/bottom shells is shorter than that to the rotor core, which leads to stator leakages between stator windings and the top/bottom shells. However, in the analytical model, the gaps are not taken into account. Therefore, the analytical result gives a larger peak value of B_θ than the numerical result.

With respect to the B_ϕ distribution in the polar areas of Fig. 12, deviations from the numerical results are due to the assumption that PMs have the same conductivity with copper. Eddy currents flowthrough there in the analytical model and generate B_ϕ in the polar area. This explanation is validated by the B_ϕ distribution got from the numerical simulation without PMs on the rotor (where the copper layer is a complete spherical shell).

In above, the dynamic field model is developed for the case where only one set of driving windings is energized and orientation of the energized winding set is specific (about the z-axis). However, the field model is also applicable to cases where more than one set of windings are energized wherever

their orientations. Due to the linearity of Laplace equations and heat diffusion equations, as well as the principle of vector superimposition, flux density distribution, or eddy currents distribution excited by two or more windings can be obtained by summing up solutions of cases where each set of windings is energized, respectively. In the case where the energized winding set is not about the z-axis, flux density distribution in the field can be obtained through coordinate conversion of results presented earlier. Furthermore, if only a few coils are energized rather than the whole winding set, the developed field model is still applicable. In that case, only the formula of the approximated surface current needs to be changed.

VI. Electromagnetic Torques and Forces

Once ac windings are activated, driving torques will be generated. They can be calculated through Maxwell stress tensor (MST) or Lorentz forces acting on the eddy currents.

1) The rotor core (Region III) is made of laminated steel. Although some eddy currents are induced there, the arm length of the generated Lorentz force is short. Consequently, the electromagnetic torque arising from these eddy currents is negligible. In the numerical model, the driving torque provided by the steel domain is only 3.5% of that generated in the copper area. Therefore, eddy currents are assumed to be induced only in the copper area

$$T_{eL} = -\int_0^{2\pi}\int_{R_b}^{R_r}\int_{\beta/2}^{\pi-\beta/2} J_\theta B_r r^3 \sin^2\theta \ \mathrm{d}\theta\mathrm{d}r\mathrm{d}\phi. \tag{24}$$

2) The MST method starts from the idea of calculating electromagnetic forces on charges in a certain volume. Through tensor arithmetic, the volume integral is converted to surface integral of local tangential stress on the boundary surface. This approach is usually used in finite element solutions, since it only requires knowledge of the local flux density distribution at the boundaries [12], [13]

$$T_{eM} = \int_0^{2\pi}\int_0^{\pi} H_\phi B_r r^3 \sin^2\theta \ \mathrm{d}\theta\mathrm{d}\phi. \tag{25}$$

When the rotor is blocked and driving windings on the equatorial plane are energized, the generated electromagnetic torque is calculated through different ways. Torque calculations based on the analytical field model and those based on the numerical field distribution are compared in Table IV, with the errors never exceeding 4%. Since the existence of PMs within the region II is not taken into account for the dynamic field modeling, the driving torques got from the analytical model are quite close to those obtained from the numerical model without PMs (where the copper layer is a complete spherical shell). The very limited deviation (<2%) is caused by the neglected stator eddy currents, which weaken the flux density in the air gap. Compared to the driving torques got from the numerical model where PMs exist (whether the remanence is set to zero or 0.23 T listed in Table II), the difference with the analytical results increases. This deviation is contributed by the existence of PMs which disturbs the circulation of eddy currents on the rotor.

TABLE IV
Comparison of Generated Electromagnetic Torques

Torques	Analytical	Numerical without PM	Numerical with PM
T_{eM}	12.18 mNm	12.17 mNm (<1%)	11.75 mNm (3.6%)
T_{eL}	12.177 mNm	12.02 mNm (1.3%)	11.7 mNm (4%)

As analyzed in Section V, the static field of PMs displaces the revolving magnetic field excited by ac currents. For instance, on the equatorial plane, the magnetic flux density on one side is stronger than that on the other side. Since eddy currents in the copper region are induced by the revolving magnetic field, the resultant Lorentz force on one side is larger than that of the opposite side. Consequently, except for driving torques, a resulting force is generated. Besides, since the flux density in one gap side is larger than the other side, a non-linear sticking force will be generated between the ferromagnetic rotor core and the stator back iron. The two factors form a radial force which is revolving at the frequency same to the input frequency of driving windings. If this disturbance force is not handle properly, it could contribute to the pointing error and be transferred to the payload, causing imaging distortion for observation missions. If the disturbance force cause resonance with on-board elements such as telescope mirrors, it could cause damages. To mitigate this disturbance force, the approach of bearing-less induction machine [33] can be adopted. Bearing coils placed coaxially with the driving coils are changed to ac fed and work as two-pol-pair three-phase windings (the frequency is double that of the driving windings). Phase angle of bearing input currents will be adjusted to make the bearing windings electrically orthogonal to the driving windings. By adjusting the ac input currents of the bearing windings, the unbalanced flux density in the opposite gap sides can be compensated.

VII. Conclusion

This paper presents the design of a reaction sphere which could perform 4π rotations. The innovative combination of PMs and electromagnetic induction enables the generation of control torques about any desired axes for spacecraft attitude control. To facilitate dynamics modeling of the actuator, analytical models have been developed to predict the magnetic flux density distribution in the superimposed field, where both PMs and alternating stator currents are involved. Especially, the improved analytical model for fields generated by stator windings provides an insight about B_θ distribution for the first time, which reveals non-negligible flux leakage in spherical actuators. Based on the obtained field information, models of the resultant torques were built up subsequently. Comparisons with the numerical results validated that the developed analytical models allow to predict the magnetic flux density distribution and driving torques precisely. Except for the analysis of the proposed reaction sphere, the analytical models are generally applicable to static and dynamic fields in spherical machines.

In the presented actuator, rotations excited by electromagnetic induction are decoupled from PMs. In principle,

its dynamics modeling can follow that of a conventional ac machine. However, due to the spherical geometry and the toroidal winding, significant leakages are expected in the actuator and require further investigations. The complete dynamics modeling of the proposed reaction sphere, as well as optimizations of involved parameters will be discussed in a future paper.

ACKNOWLEDGMENT

The work of L. Zhu was supported by China Scholarship Council.

REFERENCES

[1] W. J. Larson and J. R. Wertz, Eds., *Space Mission Analysis and Design*, vol. 1. Torrance, CA, USA: Microcosm, Inc., 1992.

[2] W. Haeussermann, "The spherical control motor for three axis attitude control of space vehicles," NASA, Washington, DC, USA, Tech. Rep. NASA TM X-50071, 1959.

[3] L. Rossini, E. Onillon, O. Chételat, and Y. Perriard, "Closed-loop magnetic bearing and angular velocity control of a reaction sphere actuator," *Mechatronics*, vol. 30, pp. 214–224, Sep. 2015.

[4] E. Stagmer, "Reaction sphere for stabilization and control in three axes," U.S. Patent 9 475 592, Oct. 25, 2016. [Online]. Available: https://www.google.com/patents/US9475592

[5] J. Doty, "Reaction sphere for spacecraft attitude control," WO Patent 029 283, Oct. 14, 2010. [Online]. Available: https://www.google.com/patents/WO2010117819A1?cl=en

[6] L. Rossini *et al.*, "Development and closed-loop experimental results of a reaction sphere elegant breadboard," in *Proc. 16th Eur. Space Mech. Tribol. Symp.*, 2015, pp. 1–6.

[7] L. Zhu, J. Guo, and E. Gill, "Review of reaction spheres for spacecraft attitude control," *Progr. Aerosp. Sci.*, vol. 91, pp. 67–86, May 2017.

[8] A. Iwakura, S. Tsuda, and Y. Tsuda, "Investigation of 3 dimensional reaction wheel," in *Proc. 57th Int. Astron. Congr. (IAC)*, Valencia, Spain, 2006, pp. 1–7.

[9] D.-K. Kim, H. Yoon, W.-Y. Kang, Y.-B. Kim, and H.-T. Choi, "Development of a spherical reaction wheel actuator using electromagnetic induction," *Aerosp. Sci. Technol.*, vol. 39, pp. 86–94, Dec. 2014.

[10] Y. Shirasawa and Y. Tsuda, "System performance analysis of three dimensional reaction wheel for the attitude control of microsatellites," *Trans. Jpn. Soc. Aeron. Space Sci.*, vol. 7, no. 26, pp. Pd_105–Pd_110, 2009.

[11] M. Kumagai and R. L. Hollis, "Development and control of a three DOF spherical induction motor," in *Proc. IEEE Int. Conf. Robot. Autom. (ICRA)*, May 2013, pp. 1528–1533.

[12] K. Davey, G. Vachtsevanos, and R. Powers, "The analysis of fields and torques in spherical induction motors," *IEEE Trans. Magn.*, vol. MAG-23, no. 1, pp. 273–282, Jan. 1987.

[13] D. Spałek, "Spherical induction motor with anisotropic rotor-analytical solutions for electromagnetic field distribution, electromagnetic torques and power losses," in *Proc. Int. Compumag Soc. Test. Electromagn. Anal. Methods (TEAM)*, vol. 34, 2007, pp. 1–12.

[14] J. F. P. Fernandes, V. M. Machado, and P. J. C. Branco, "Magnetic field analysis in shell-like spherical induction machines with zenithal traveling waves," *IEEE Trans. Energy Convers.*, vol. 32, no. 3, pp. 1081–1089, Sep. 2017.

[15] P. Vijayraghavan and R. Krishnan, "Noise in electric machines: A review," in *Proc. 33rd IAS Annu. Meeting IEEE Ind. Appl. Conf.*, vol. 1, Oct. 1998, pp. 251–258.

[16] J. Liu, H. Deng, C. Hu, Z. Hua, and W. Chen, "Adaptive backstepping sliding mode control for 3-DOF permanent magnet spherical actuator," *Aerosp. Sci. Technol.*, vol. 67, pp. 62–71, Aug. 2017.

[17] H.-I. Lee and M. D. Noh, "Optimal design of toroidally-wound brushless DC machines," in *Proc. IEEE Int. Conf. Ind. Technol. (ICIT)*, Feb. 2009, pp. 1–5.

[18] H.-I. Lee, S.-Y. Yoo, and M. D. Noh, "Toroidally-wound self-bearing BLDC motor with Lorentz force," *IEEE Trans. Magn.*, vol. 46, no. 6, pp. 2148–2151, Jun. 2010.

[19] A. Schwab, *Field Theory Concepts: Electromagnetic Fields. Maxwell's Equations Grad, Curl, Div. Etc. Finite-Element Method. Finite-Difference Method. Charge Simulation Method. Monte Carlo Method*. Berlin, Germany: Springer, 2012.

[20] M. Curti, J. J. H. Paulides, and E. A. Lomonova, "An overview of analytical methods for magnetic field computation," in *Proc. 10th Int. Conf. Ecol. Vehicles Renew. Energies (EVER)*, Mar./Apr. 2015, pp. 1–7.

[21] K.-M. Lee, H. Son, and K. Bai, "Image method with distributed multipole models for analyzing permanent-magnet-based electromagnetic actuators," in *Proc. ASME Dyn. Syst. Control Conf.*, 2008, pp. 1083–1089.

[22] B. Li, G.-D. Li, and H.-F. Li, "Magnetic field analysis of 3-DOF permanent magnetic spherical motor using magnetic equivalent circuit method," *IEEE Trans. Magn.*, vol. 47, no. 8, pp. 2127–2133, Aug. 2011.

[23] L. Yan, D. Liu, Z. Jiao, C. Y. Chen, and I. M. Chen, "Magnetic field modeling based on geometrical equivalence principle for spherical actuator with cylindrical shaped magnet poles," *Aerosp. Sci. Technol.*, vol. 49, pp. 17–25, Feb. 2016.

[24] W. Xiuhe, *Permanent magnet Machines*. Beijing, China: China Power Press, 2007.

[25] Z. Q. Zhu, D. Howe, and C. C. Chan, "Improved analytical model for predicting the magnetic field distribution in brushless permanent-magnet machines," *IEEE Trans. Magn.*, vol. 38, no. 1, pp. 229–238, Jan. 2002.

[26] D. Lide, "Magnetic susceptibility of the elements and inorganic compounds," in *Handbook of Chemistry and Physics*. Boca Raton, FL, USA: CRC Press, 2005, pp. 134–139.

[27] J. D. Jackson, *Classical Electrodynamics*. Hoboken, NJ, USA: Wiley, 2007.

[28] G. Arfken and H. Weber, *Mathematical Methods For Physicists*. New York, NY, USA: Elsevier, 2005. [Online]. Available: https://books.google.nl/books?id=tNtijk2iBSMC

[29] L. Yan, I. Chen, C. Lim, G. Yang, and K. Lee, *Design, Modeling and Experiments of 3-Dof Electromagnetic Spherical Actuators*. Dordrecht, The Netherlands: Springer, 2011. [Online]. Available: https://books.google.nl/books?id=WcFqJ1LNxtwC

[30] W. Smythe, *Static and Dynamic Electricity*. New York, NY, USA: Hemisphere Publishing, 1988.

[31] G. Mrozynski and E. Baum, "Analytical determination of eddy currents in a hollow sphere excited by an arbitrary dipole," *IEEE Trans. Magn.*, vol. 34, no. 6, pp. 3822–3829, Nov. 1998.

[32] M. Strumik *et al.*, "Analytical model of eddy currents in a reaction sphere actuator," *IEEE Trans. Magn.*, vol. 50, no. 6, Jun. 2014, Art. no. 4004607.

[33] A. Chiba, T. Fukao, O. Ichikawa, M. Oshima, M. Takemoto, and D. G. Dorrell, *Magnetic Bearings and Bearingless Drives*. New York, NY, USA: Elsevier, 2005.